# Unveiling Enhanced Electrostatic Repulsion in Silica Nanosphere Assembly: Formation Dynamics of Body-Centered-Cubic Colloidal Crystals

*Qingsong Fan[1], Zhiwei Li[1], Yichen Li[1], Aiqin Gao[1], Yuzhi Zhao[1], Daniel Yang[1], Chenhui Zhu[2], Tatiana V. Brinzari[3], Guofeng Xu[3], Long Pan[3], Luat T. Vuong[4], Yadong Yin[1*]*

1: Department of Chemistry, University of California, Riverside, CA 92521, USA
2: Advanced Light Source, Lawrence Berkeley National Laboratory, Berkeley, CA 94720, USA
3: Colgate-Palmolive Company, Piscataway, New Jersey 08854, United States
4: Department of Mechanical Engineering, University of California, Riverside, CA 92521, USA
*Email: yadongy@ucr.edu

Keywords: colloidal photonic crystals, silica nanospheres, electrostatic repulsion, assembly dynamics, body-centered cubic, electrical double layer

## Abstract

We demonstrate the effective establishment of long-range electrostatic interactions among colloidal silica nanospheres through acid treatment, enabling their assembly into colloidal crystals at remarkably low concentrations. This novel method overcomes the conventional limitation in colloidal silica assembly by removing entrapped $NH_4^+$ ions and enhancing the Electrical Double Layer (EDL) thickness, offering a time-efficient alternative to increase electrostatic interactions compared to methods like dialysis. The increased EDL thickness facilitates the assembly of $SiO_2$ nanospheres into a body-centered cubic lattice structure at low particle concentrations, allowing for broad spectrum tunability and high tolerance to particle size polydispersity. Further, we uncover a disorder-order transition during colloidal crystallization at low particle concentrations, with the optimal concentration for crystal formation governed by both thermodynamic and kinetic factors. This work not only provides insights into assembly mechanisms but also paves the way for the design and functionalization of colloidal silica-based photonic crystals in diverse applications.

## Introduction

It has been known since the 1970s that highly charged, monodisperse colloidal nanoparticles could self-assemble into highly ordered, non-close-packed 3D crystalline superlattices, often referred to as colloidal photonic crystals.[1-7] Due to their non-close packing structure, the interparticle distance can be conveniently tuned by simply adjusting the concentration of the colloidal solution. Consequently, the wavelength of the corresponding light diffraction shifts, giving rise to varied colors. Such a stimuli-responsive color shift property has been exploited in various applications, including metal ion indicators,[8-12] glucose detection,[13, 14] force sensor,[15] mesopore detection,[16] etc.

Monodispersed nanospheres are considered the best building blocks for fabricating colloidal photonic crystals due to their ease of production, uniform size, and high symmetry. Among various materials, polystyrene (PS) and $SiO_2$ nanospheres have been most extensively utilized for their reliable synthesis methods (i.e., emulsion polymerization[17, 18] and sol-gel process (Stöber method)[19, 20]), producing colloidal crystals with excellent photonic properties. Decades of investigation have revealed that the ordered self-assembly of these highly charged nanospheres in solution is driven by minimizing the free energy arising from electrostatic repulsive interactions.[2, 21] Although there is no clear distinction, the reported systems can be roughly classified by the required volume fraction of the colloidal solution. Some systems only show photonic crystals assembled at high volume fractions (i.e., > 30 vol.%),[12, 15, 16, 22, 23] while others do not require such a high concentration (i.e., ~1-15 vol.%).[2, 4, 7] As the ordering of nanoparticles results from the electrostatic repulsion, the required volume fraction reflects the effective range of this interaction, which is determined by the thickness of the electrical double layers (EDL).

Although the self-assembly of PS nanospheres in low-volume fraction solutions has been reported,[2-5, 8, 21, 24, 25] assembling $SiO_2$ nanospheres typically requires high-volume fraction solutions, indicating the lack of sufficiently long-range electrostatic repulsion.[12, 15, 16, 23] This raises the question of why colloidal $SiO_2$ nanospheres have difficulty obtaining a thick EDL. In this study, by examining the chemical structure of $SiO_2$ nanospheres synthesized by the Stöber method, we show that trapped $NH_4^+$ ions in the $SiO_2$ core were the cause of the issue. We further demonstrate that ion exchange by simple acid treatment can effectively remove the trapped $NH_4^+$ ions and prevent their release to the solution, reducing the ionic strength of the solution and facilitating the acquisition of a thick EDL for $SiO_2$ nanospheres. This method allows the successful assembly of

$SiO_2$ nanospheres into photonic crystals under low dispersion concentrations in the range of ~1-5 vol.%, comparable to the lowest value reported for PS.[2] This long-range electrostatic repulsion enables two significant features: (1) The diffraction peak can be tuned from visible to the near-infrared regime, displaying a wide tunability of ~250 nm, and (2) colloidal photonic crystals are still observable even for a mixture of $SiO_2$ nanospheres with two distinct sizes (87 nm and 120 nm), making it less stringent on the uniformity of the building blocks for the assembly. In contrast to previous studies that primarily focused on the optical and structural properties of colloidal crystals, this research delves into the assembly dynamics for the first time, uncovering the concentration dependence of crystal formation rate.

A key finding of our research is that crystallization involves a disorder-order transition without any significant change in density, a conclusion that sets it apart from previous studies. Utilizing numerical simulation, we further show that the optimal concentration for crystal formation is governed by both thermodynamic and kinetic factors: a large interparticle separation at too-low concentrations hampers the maintenance of effective crystal lattice, whereas too-high concentrations raise the kinetic energy barrier for defect correction. Our findings provide new insights into the mechanisms underlying the colloidal self-assembly and have important implications for the design and optimization of silica-based photonic crystals.

## Results and Discussion

$SiO_2$ nanospheres with a diameter of ~90 nm were synthesized by the classical Stöber method.[19] In a typical process, $NH_4OH$ is required as a catalyst to promote the hydrolysis of tetraethyl orthosilicate (TEOS). In a previous study, Chen et al. observed inhomogeneity in the resulting $SiO_2$ nanospheres and attributed it to the precipitation of ion-paired polyelectrolytes.[26, 27] According to this hypothesis, the core of $SiO_2$ consists of long poly(silicic acid) chains with a large amount of $[-(SiO^-)(NH_4^+)]$ ion pairs, while the shell consists of more condensed, short chains. The presence of $NH_4^+$ ions in the core was supported by the observation of a high N/Si element ratio (2-5 %).[27] When these $SiO_2$ nanospheres are redispersed in water, the reaction between the ion pair and nearby [-Si-OH] produces $NH_4OH$ (Figure 1a), which results in an alkaline solution with a high ionic strength. The reaction between the ion pair and [-Si-OH] is slow under room temperature, which explains why the pH and electrical conductivity of the colloidal dispersion of $SiO_2$ remain high even after being purified with water three times (Figure 1b and 1c, untreated sample).

The trapped $NH_4^+$ could be partially replaced by $H^+$ through mass action by stirring the $SiO_2$ nanospheres in an HCl solution. After purification, when the acid-treated $SiO_2$ nanospheres were dispersed in water, the condensation reaction yielded $H_2O$ instead of $NH_4OH$ (Figure 1b). As a result, the conductivity of the colloidal dispersion did not increase significantly, indicating a low ionic strength. The reduced ionic strength significantly augmented the EDL thickness and sustained the electrostatic repulsion between nanospheres across substantial distances, extending beyond three times the nanosphere diameter.

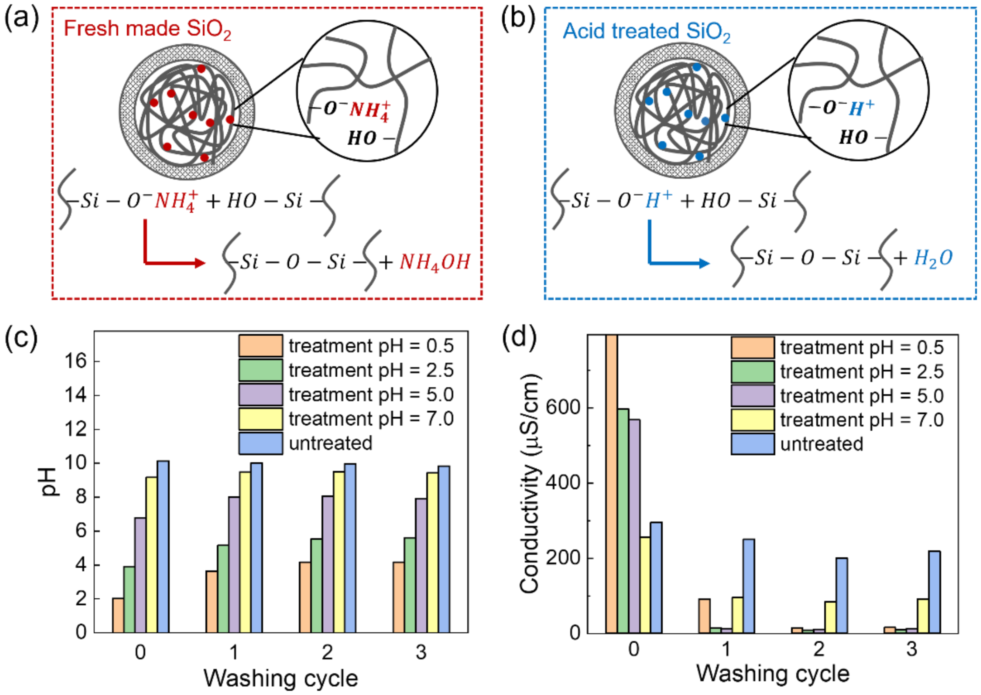

**Figure 1.** Enhanced electrostatic interparticle repulsion by acid treatment. (a, b) Scheme illustrating reduced ionic strength of the $SiO_2$ colloidal dispersion through the acid treatment. (c, d) pH (c) and conductivity (d) of the colloidal $SiO_2$ dispersions upon repeated washing, with the legend denoting the pH values of the dispersion after adding the acid.

To determine the optimal condition for acid treatment, we added HCl solutions (1 M) of varied volumes to the dispersions of freshly made $SiO_2$ nanospheres to reach different pH values. Figures

1b and 1c show that the trapped $NH_4^+$ ions could be sufficiently replaced by $H^+$ only when the treatment pH was low (i.e., 0.5 and 2.5), as indicated by the low pH values and conductivities after washing. In contrast, samples with treatment pH values of 5.0 and 7.0 retained pH values greater than 7 even after washing. The low ionic strength resulting from acid treatment promoted the electrostatic interaction among the nanospheres over longer distances, facilitating their assembly in water at low concentrations and leading to the formation of photonic crystals. Specifically, as shown in Figure 2, nanospheres with a treatment pH of 0.5 exhibited assembled photonic crystals at concentrations ranging from 7.70 wt.% to 12.95 wt.%, corresponding to the diffraction peaks from 440 nm to 525 nm. The sample treated with a pH of 2.5 showed a wider range of concentrations for assembly, from 4.46 wt.% to 9.90 wt.%, due to its lower ionic strength than the sample treated with more $H^+$. In contrast, no crystalline assemblies could be observed at similar particle concentrations for samples with higher treatment pH values.

In principle, the electrostatic force driving the nanosphere assembly is affected by both surface charge and ionic strength. However, the acid treatment did not significantly alter the surface charge of the $SiO_2$ nanospheres, as evidenced by the zeta potential measurements (Figure S1). Therefore, the concentration range suitable for assembly is believed to directly relate to the ionic strength of the colloidal dispersion. The optimal sample (with treatment pH of 2.5), having the lowest ionic strength, exhibited a crystalline appearance with a concentration as low as 4.46 wt.%, corresponding to an average center-to-center distance of ~280 nm, which is more than two times the nanosphere diameter. It should be noted that although the sample with a treatment pH of 5 exhibited a low conductivity value, its ionic strength remained relatively high. This is due to the substantial amount of $OH^-$ it contains, which has lower mobility and is nearly twice as slow as $H^+$.

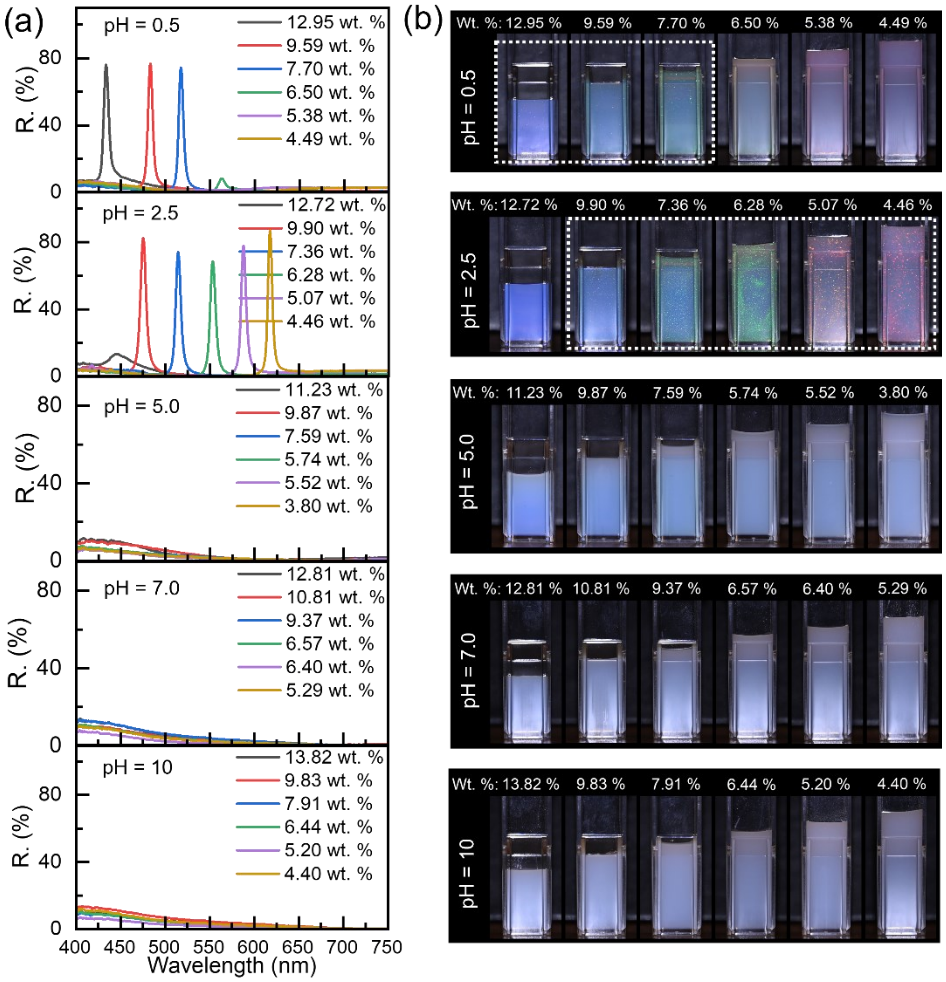

**Figure 2.** Assembly behaviors of aqueous dispersions of $SiO_2$ nanospheres pre-treated at varied pH. (a) Reflection spectra of the colloidal dispersions with different concentrations. (b) Digital photos of the colloidal dispersions with different concentrations, with dashed boxes highlighting the dispersions with apparent crystalline appearances. The cuvette width is 1 cm.

The electrostatic interaction among nanoparticles for driving the assembly of photonic crystals is effective even when the separation exceeds 300 nm (resulting in a diffraction wavelength > 700 nm). Figure 3a shows the appearance of dispersions of $SiO_2$ nanospheres (average diameter: 84 nm, treatment pH of 2.5) of different concentrations. At concentrations higher than 12 wt.%, the samples exhibited only a uniform blue color, and no crystalline domains were observed under a dark-field optical microscope (Figure 3d and Figure S2). The reflection spectra of two high-concentration samples (12.43% and 16.31%) displayed broad peaks with lower intensities than other samples (Figure 4a, top). Despite their lack of iridescent appearance, high-concentration samples still exhibited angle-dependent color change (Figure 3e), which is distinct from the “photonic glass” known for its short-range order.[28-30] As such, we refer to these two samples as “defective crystals” because long-range order was still present, but the presence of many defects significantly broadened the diffraction peak.

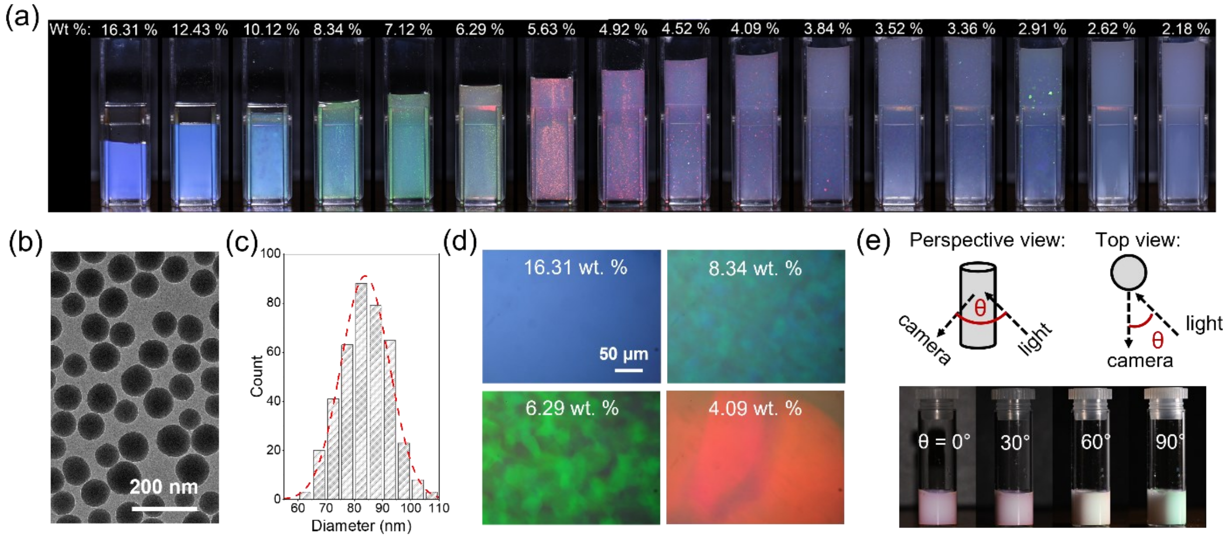

**Figure 3.** Optical properties of assembled colloidal crystals. (a) Digital photos showing the appearances of colloidal dispersions of $SiO_2$ nanospheres (84 nm ± 9 nm) with varied concentrations. (b, c) Transmission Electron Microscope (TEM) image and size distribution plot of the $SiO_2$ nanospheres. (d) Dark-field optical microscopy images of colloidal assemblies of $SiO_2$ nanospheres of various concentrations. (e) Angle-dependent color change of the sample in the “defective crystal” state ($SiO_2$ diameter: 120 nm, 16.09 wt.%), with the top scheme illustrating the arrangement of the incident light and camera.

The crystalline domains could be observed when the nanosphere concentration was between 10.12 wt.% and 2.91 wt.%. The diffraction wavelength exhibited a continuous red shift as the concentration decreased, while two peaks appeared in the reflection spectra, with the secondary peak having a lower intensity and shorter wavelength than the primary peak (Figure 4a, bottom). When $SiO_2$ nanospheres larger than 100 nm were used as building blocks (Figures S3-S5), the reflection spectra showed a maximum of four diffraction peaks within the spectrometer limit, and the wavelengths of these peaks followed the ratio of $\frac{1}{\lambda_1}:\frac{1}{\lambda_2}:\frac{1}{\lambda_3}:\frac{1}{\lambda_4} \approx 1:\sqrt{2}:\sqrt{3}:2$. Previous studies have suggested that the assembled crystals possess either a face-centered-cubic (FCC) or body-centered-cubic (BCC) structure, depending on the experimental conditions, by analyzing the Kossel rings generated by light diffraction.[4, 21, 24, 25] By examining the possible diffraction wavelengths from different crystal planes of both FCC and BCC structures (Table S1), we concluded that our crystals were made of BCC lattices with the four diffraction peaks corresponding to (110), (200), (211) and (220) planes (Figure 4c). Our numerical simulation results indicated that the BCC lattice is the consequence of the thick EDL of the nanoparticles, as explained in more detail later.

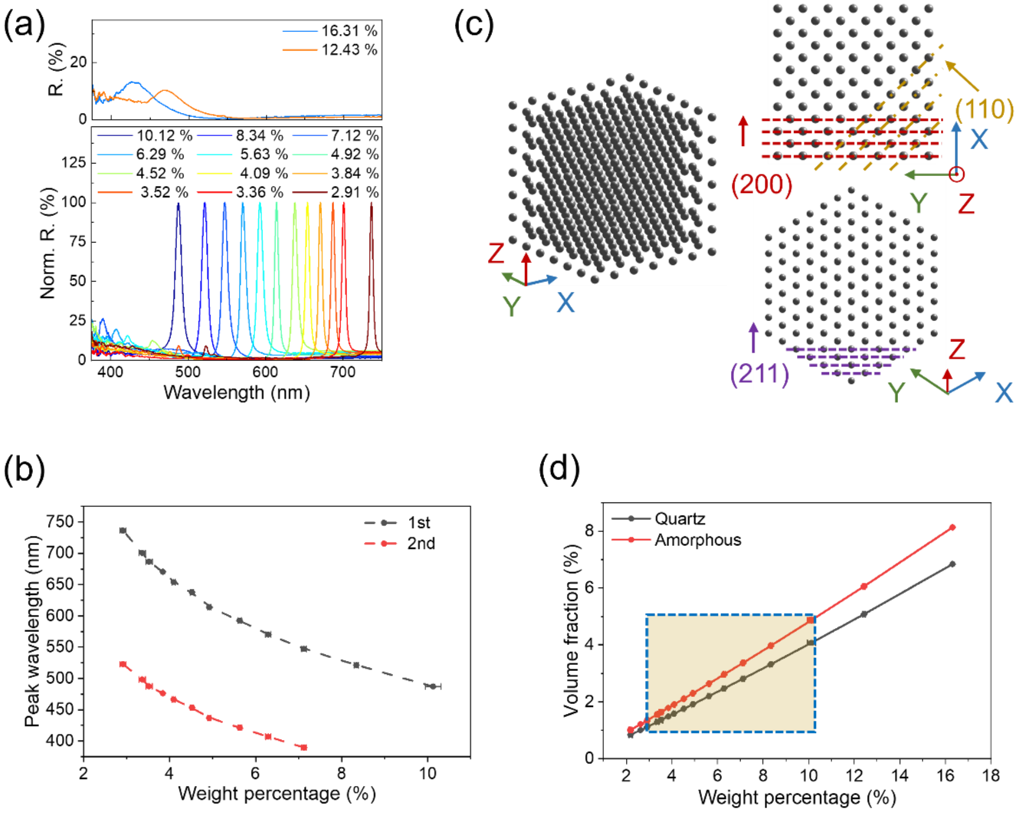

**Figure 4.** Optical and structural analysis of colloidal crystals assembled from 84 nm $SiO_2$ nanospheres. (a) Reflection spectra of dispersions in Figure 3a. (b) Plot of diffraction wavelength vs. concentration. (c) Schematic illustration of 3D BCC lattice and crystal planes. (d) Calculated

volume fraction vs. the measured weight percentage. The area in the square represents the range within which the dispersions appear crystalline.

The long-range electrostatic interaction between nanospheres offers the opportunity to assemble photonic crystals at significantly lower concentrations than previous $SiO_2$ nanosphere-based systems. The calculated volume fraction of dispersions with assembled crystals ranges from ~1 vol.% to ~5 vol.%, based on the density of amorphous and crystalline $SiO_2$ (Figure 4d). In contrast, the typical lowest concentration required for $SiO_2$ nanosphere assembly is ~30 vol.%.[12, 15, 16, 23] Additionally, it enables the fabrication of photonic crystals with the same color using nanospheres of a much smaller size (84 nm vs. 190 nm).

The assembled structure of the colloidal photonic crystals was further confirmed using synchrotron-based small-angle X-ray scattering (SAXS) analysis. The 2D SAXS patterns of two samples were obtained (Figure 5a): one with assembled crystals (13.83 wt.%, see Methods section for an explanation of crystallization at an increased concentration) and another with only defective crystals (21.20 wt.%), both assembled from $SiO_2$ nanospheres with a diameter of 84 nm. In contrast to the sample with defective crystals that showed diffraction rings, the sample with photonic crystals exhibited distinct diffraction spots. The lattice structure was identified by analyzing the peaks in the 1D SAXS data obtained by azimuthal averaging the 2D scattering patterns. As shown in Figure 5b, the experimental 1D SAXS data closely matched the simulated SAXS data of a BCC lattice with a lattice constant of 224 nm. The simulated structure factor of this BCC lattice revealed that the observed peaks in the experimental curve corresponded to the (110), (200), and (211) planes. In contrast, the simulated SAXS data of an FCC lattice with the same lattice constant did not match the experimental curve (Figure 5c), indicating the absence of an FCC lattice in the solution. For the sample with a high concentration of 21.20 wt.%, although the (110) peak was discernible, the other two peaks were not fully developed, further confirming that a high particle concentration leads to the formation of defective crystals.

The experimental 1D SAXS data of colloidal dispersions with other concentrations are shown in Figure 5e. It is evident that as the particle concentration decreases, the diffraction peaks gradually shift towards smaller q values, indicating a larger lattice constant. All the experimental data agree with the simulated curves based on a BCC lattice (Figure S6). The average nanoparticle separations, calculated using data from different measurements such as volume fraction, optical diffraction, and SAXS, are summarized in Figure 5f (see Methods section and SI). It can be observed that the results are similar throughout all concentrations, indicating that the crystalline domains possess the same density as the surrounding amorphous region, if present. This finding implies that the assembly of photonic crystals only involves a disorder-order transition without significant change in particle density, representing a conclusion that is distinct from previous studies.[4, 15]

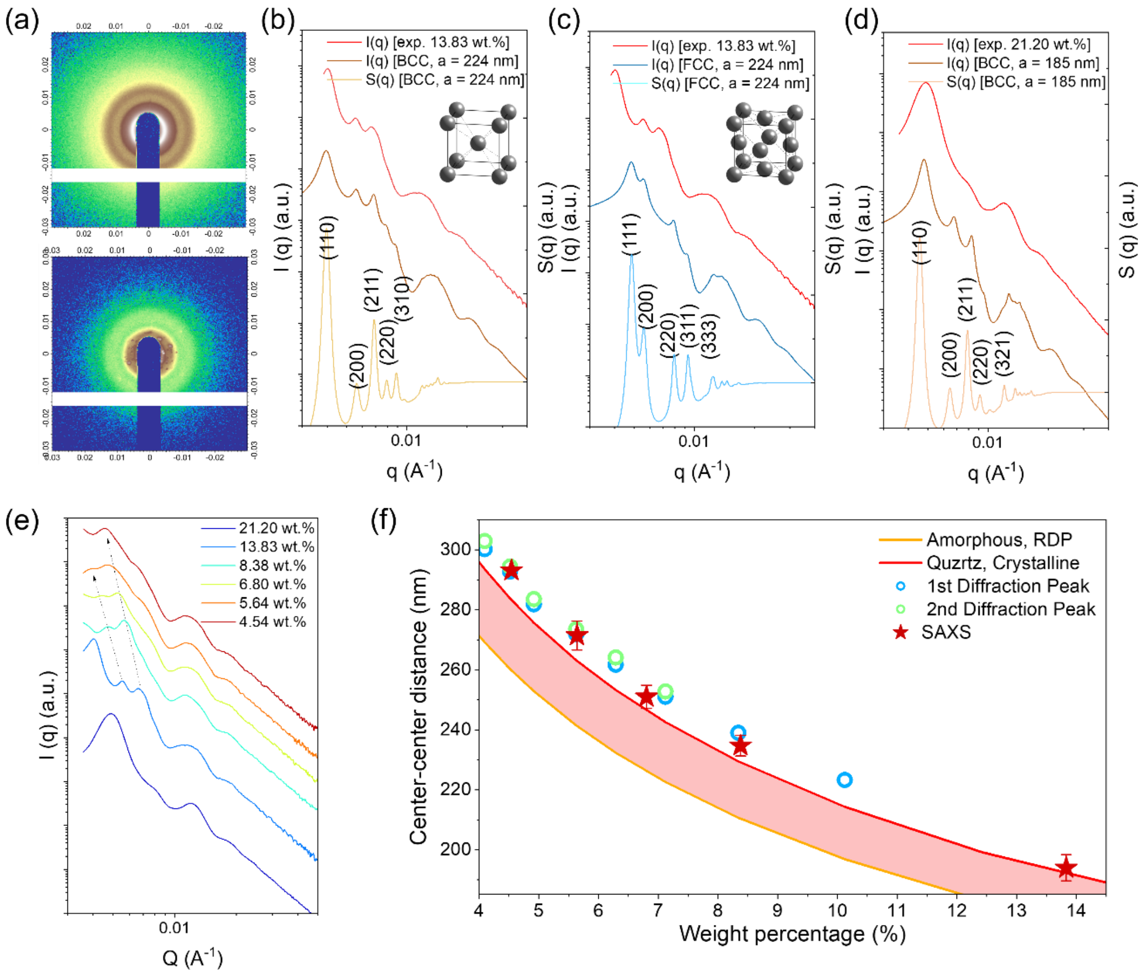

**Figure 5.** Structural analysis of the assembled colloidal crystals. (a) 2D SAXS patterns (top: 21.20 wt.%, bottom: 13.83 wt.%). (b-d) Experimental and simulated 1D SAXS patterns and structural factors for the sample with a concentration of 13.83 wt.% (b, c) and 21.20 wt.% (d), with crystal lattices in the simulation being BCC (b, d) and FCC (c). (e) Experimental 1D SAXS patterns of

samples with different concentrations. (f) Center-to-center distance calculated based on the diffraction wavelength at varying weight percent. (the orange and red lines represent the center-center distance of the two nearest particles calculated using the density of amorphous silica in a random dense packing (RDP) and quartz in a crystalline packing, respectively).

The assembled colloidal photonic crystals display sensitivity to motion and can be disintegrated by pipetting, but the nanospheres quickly reassemble into their initial states (Figures 6a, 6b, and Video S1). The assembly rates of samples with different concentrations vary, with the assembly process taking ~12 s for the dispersion with a concentration of 6.29 wt.% and ~52 s for the dispersion with a concentration of 3.84 wt.%. Here, the assembly time is defined as the time taken for the intensity to reach 90% of the maximum, see Figures 6c and 6d. Figures 6e and 6f show the time-dependent intensity change for samples with different concentrations and the relationship between assembly time and concentrations. The results show a "V" shaped curve, indicating an optimum concentration for assembly dynamics. Both higher and lower concentrations lead to prolonged assembly times.

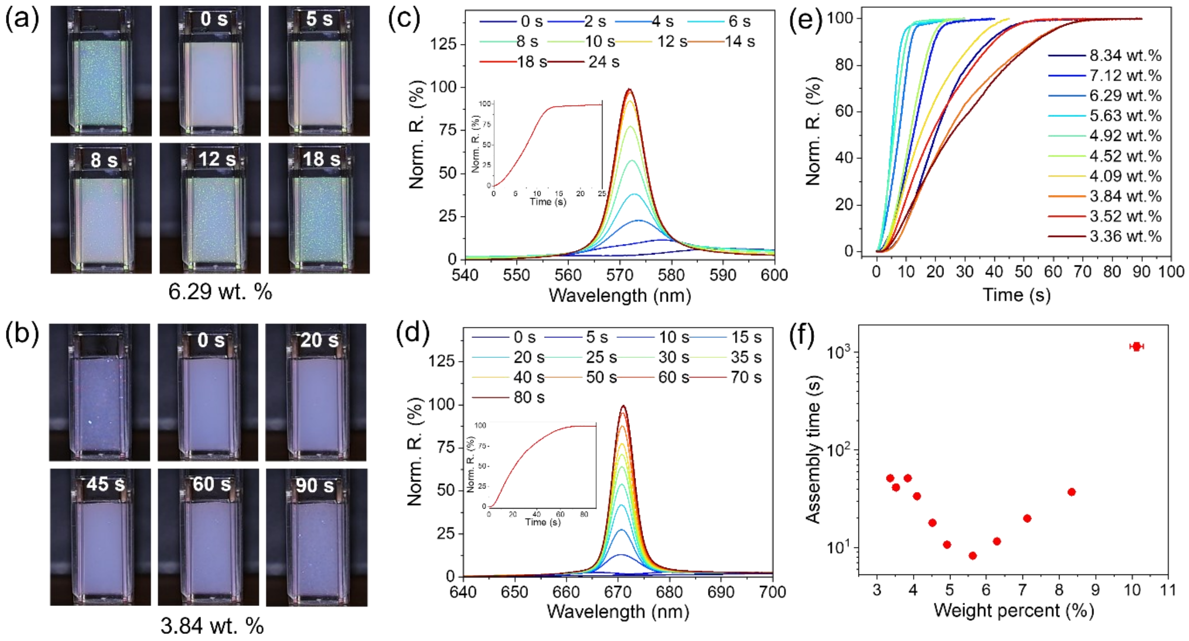

**Figure 6.** Concentration-dependent assembly dynamics of the colloidal crystals. (a, b) Digital photos showing two dispersions of $SiO_2$ nanosphere assemblies in response to agitation: 6.29 wt.%

(a), 3.84 wt.% (b). (c, d) Time-dependent reflection spectra during the assembly process for dispersions with concentrations of 6.29 wt.% (c) and 3.84 wt.% (d). The insets show the corresponding plots of intensity change vs. time at their respective diffraction wavelengths. (e, f) Plot of intensity change vs. time (e) and the corresponding assembly time (f) for dispersions with different concentrations.

To gain a deeper understanding of the assembly behaviors of the colloidal photonic crystals, we have calculated the potential energies of nanospheres and analyzed the assembly mechanism from an energetic perspective since the disorder-order transition is a potential energy-drive assembly process. Three pairwise interactions among nanospheres, namely electrostatic interaction, van der Waals interaction, and steric interaction, were considered (see Methods section for details) using parameters close to our experimental conditions ($\psi$ = -80 mV, $c = 10^{-5}$ M, $r$ = 42 nm). The electrostatic potential dominates when the center-to-center distance between two nanospheres is within 100-300 nm (Figure S8), serving as the driving force for the assembly. Unlike other forces, the electrostatic forces among nanoparticles in colloidal solution are highly sensitive to ionic strength, and the screening effect of the extra ions in the surroundings can significantly reduce the effective distance. As shown in Figure 7a, when the ionic concentration is increased from $10^{-5}$ M to $10^{-3}$ M, the total potential between two nanospheres drops more quickly as the distance increases, demonstrating that low ionic strength is essential to maintain long-range electrostatic interaction.

A BCC unit cell shown in Figure 7b was further examined. The unit cell consists of eight nanospheres at the corners of the unit cell and one at the center. The nanosphere at the center was moved manually in the $z = 0$ plane, and the energy of the centered nanosphere was calculated at different locations. Figure 7c compares the energy of the middle nanosphere when it is moved in the plane to that of the original BCC unit cell with a volume fraction of $\phi = 3\%$. The results indicate that the middle nanosphere has the lowest energy when it is in the center, and its energy increases as it moves away, forming a 2-dimensional potential well. The dashed circle represents the location where the energy difference is equal to $k_B T$, which is roughly the range (defined as the potential well width) within which the middle nanosphere can move freely due to thermal agitation after being trapped in the potential well. As expected, the potential well width is dependent on the surface potential of the nanospheres and the ionic concentration of the solution, with a larger potential well width at higher ionic concentrations in solution or lower surface potentials of the nanospheres (Figure 7d, S9 and S10).

A 1D potential well can be obtained when the middle nanosphere is moved along the $y = 0$ line on the plane depicted in Figure 7c. When considering an isolated unit cell, this 1D potential well takes on the shape of an "M" as shown in Figure 7e, and the difference in energy between its maximum and minimum represents the energy barrier that a nanosphere must surmount in order to enter or exit the unit cell. This energy barrier increases as the concentration of the colloidal dispersion increases. As discussed below, defects are generated during assembly, necessitating the nanospheres to shift between unit cells to correct these defects. As a result, this energy barrier represents the degree of difficulty in correcting defects during assembly, similar to the Ehrlich-Schwoebel barrier that a surface atom must overcome during the diffusion process.[31, 32]

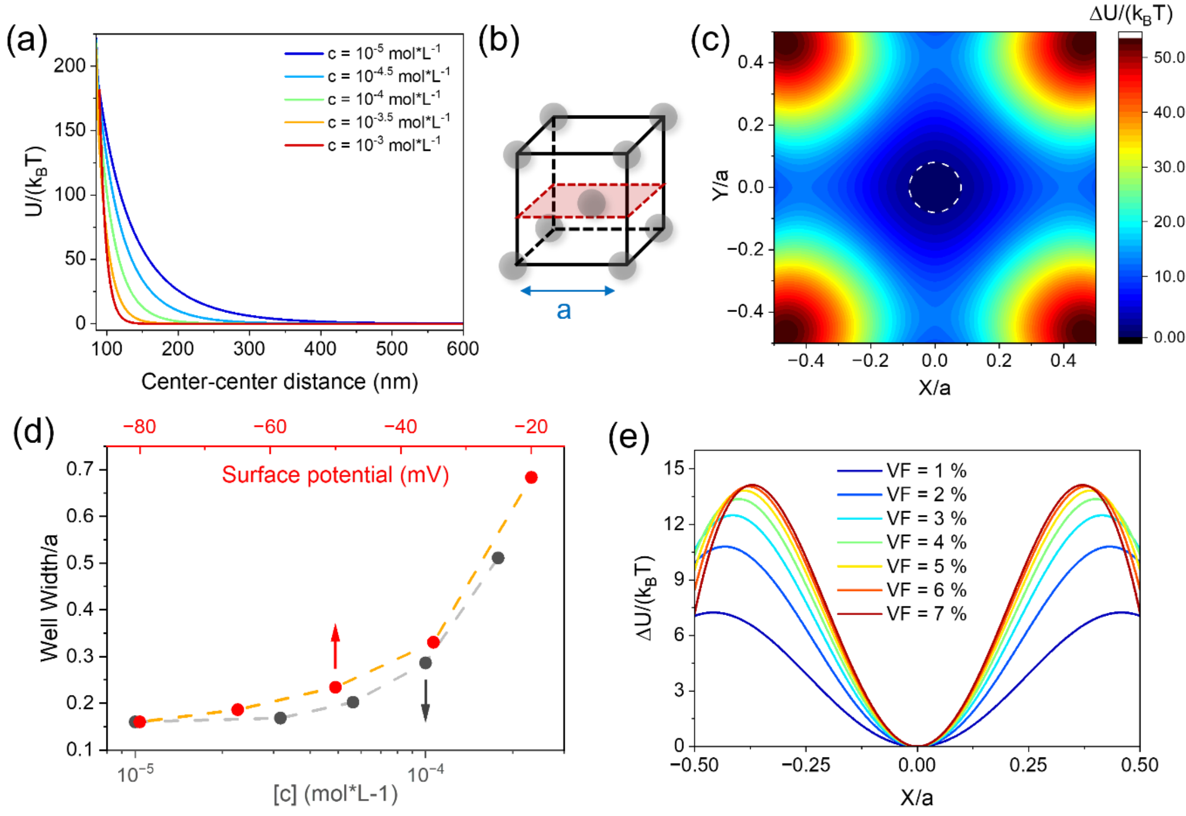

**Figure 7.** (a) Overall potential of two nanospheres ($\psi$ = -80 mV) as a function of center-to-center distance in solutions with different ionic concentrations. (b) Schematic illustration of the 2D

potential well in a BCC unit cell. (c) Potential difference mapping of the middle nanosphere in $z$ = 0 plane and at the origin ($\psi$ = -80 mV, $c$ = $10^{-5}$ M, $\phi$ = 3 vol.%). (d) The relation between reduced well width and ionic concentration, surface potential. (e) Potential difference of the middle nanosphere in the line ($y$ = 0, $z$ = 0) and at the origin ($\psi$ = -80 mV, $c$ = $10^{-5}$ M for all concentrations).

To comprehend why the disorder-to-order transition is a spontaneous process, we calculated the potential energy of a disturbed BCC lattice containing 341 nanospheres. The disturbance was introduced by randomly displacing each nanosphere in the original BCC lattice, and the degree of disturbance was controlled by a parameter called randomness (see Methods section, Figures 8a and S12). Figure 8b shows that the disturbed lattice has a higher potential energy than the original BCC lattice for each concentration, and the energy difference increases as the disturbance becomes more pronounced. This implies that the disorder-to-order transition occurs spontaneously to minimize the potential energy of the system, which is consistent with the conclusion from other studies.[2, 21] Furthermore, the assembly tendency is represented by the slope of the curve in Figure 8b, which increases with increasing concentration. Combining the results in Figures 7e and 8b, one can see that the optimum concentration for fast assembly results from the balance between thermodynamics and kinetics. High-concentration samples have a higher assembly tendency but also higher energy barriers during defect correction, while low-concentration samples exhibit the opposite behavior. When the concentration is too high, nanospheres are unable to overcome the energy barrier, resulting in the formation of defective crystals.

In this study, we utilized a considerably large system to investigate the differences between FCC and BCC lattices for nanospheres with thick and thin EDL. The system comprises 1688 nanospheres for FCC and 1729 nanospheres for BCC lattices, respectively (Figure S13). The simulation outcomes revealed that at a low ionic concentration ($c$ = $10^{-5}$ M, and corresponding $\kappa^{-1}$ = 96.3 nm), each sphere in the BCC lattice has a lower potential energy than in FCC. However, when the ionic concentration is high ($c$ = $10^{-3}$ M, corresponding $\kappa^{-1}$ = 9.63 nm), the opposite result was obtained (Figure 8c). The potential of each sphere in the lattice is determined by the coordination number (CN) and the nearest interparticle separation. Although for the same volume fraction, FCC has a larger nearest interparticle separation than BCC (FCC/BCC = 1.0287), BCC has a smaller CN than FCC (BCC: 8; FCC: 12). When the ionic concentration is low, the energy difference induced by the interparticle separation is small compared to that induced by the CN since the potential energy changes less steeply with distance. Thus, the BCC lattice, having a smaller CN, is more stable under thick EDL conditions. Conversely, at high ionic concentrations, the energy difference induced by the interparticle separation dominates. Thus, the FCC lattice, having a larger interparticle separation, becomes more stable under thin EDL conditions. This conclusion is consistent with several theoretical and experimental results, regardless of the different methods employed.[4, 33-35]

As proof of concept, we utilized a coarse-grained model to study the assembly dynamics (see Methods section). The model involved randomly distributed 559 nanospheres within a simulation box that was bounded on all sides. Throughout the course of the dynamic simulation, we tracked the position of each nanosphere at every moment in time. As time progressed, the energy of the system decreased as well as the reduced standard deviation (std/lattice constant) of the positional differences (distance between the current position and final equilibrium position), and eventually oscillated around its minimum due to the Brownian motion (Figure 8d). The change in slope of the time-dependent standard deviation was indicative of a defect correction process, as shown in Video S2, and served as a clearer indicator of when the assembly process had been completed. It is worth noting that the timescale of the simulation for assembly was 2-3 orders of magnitude smaller than that of experimental results. We attribute this discrepancy to the limited size of the simulated system: as the number of simulated nanoparticles increases, (1) the chance of formation of defects increases (Figure S14), (2) the influence of the additional boundary condition (see Methods section) decreases. Despite this timescale disparity, the simulated assembly time versus concentration yielded a similar "V"-shaped curve as shown in Figure 8e.

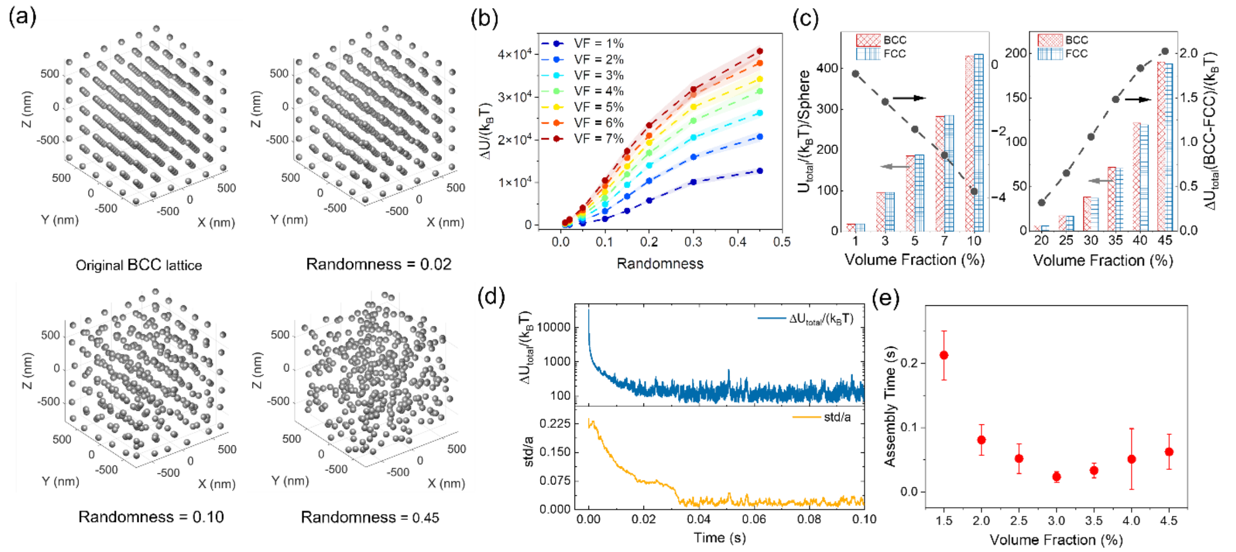

**Figure 8.** (a) Configurations of the BCC lattice with different randomness values. (b) Potential difference between distorted lattices with different randomness and original BCC lattice. (c) Potential energies of each sphere in BCC and FCC lattices under different ionic concentrations: $c = 10^{-5}$ M (left) and $10^{-3}$ M (right). (d) The change of potential energy and standard deviation of the displacements during a dynamic assembly process ($\psi$ = -80 mV, $c = 10^{-5}$ M, $\phi$ = 3 vol.%). (e) Plot of simulated assembly time vs. concentration of the colloidal dispersion.

The assembly of colloidal photonic crystals resembling those previously observed can be seen in $SiO_2$ nanospheres of larger sizes (102 nm, 120 nm, and 140 nm in diameter) treated with a pH of 2.5, as shown in Figure 9a and Figures S3-S5. These crystals exhibit similar optimal concentration ranges for assembly (~3 to ~10 wt.%), suggesting that the acid treatment is a general method for obtaining a thick EDL for $SiO_2$-based particles. The wide tuning range of the primary diffraction wavelengths (~250 nm) seen in Figure 9b is attributed to the long-range electrostatic repulsion, which gives the nanoparticles enough space to adjust their separation. Additionally, after being treated with acid, $SiO_2$ nanospheres with a much larger size (average diameter: ~ 350 nm) exhibited assembled crystal structures at concentrations as low as 8.77 wt.% (Figure S16), further demonstrating the universality of this method.

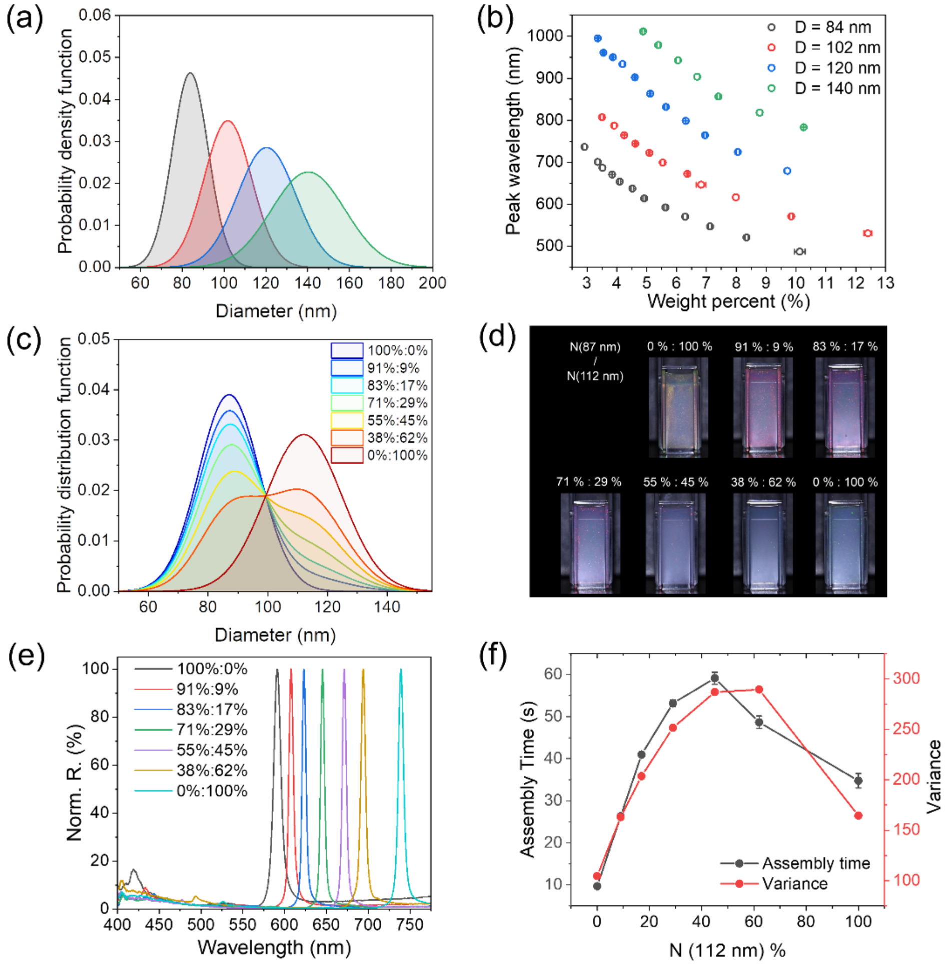

**Figure 9.** (a) Fitted probability density function of $SiO_2$ nanospheres with different diameters. (b) The relation between primary diffraction wavelengths and concentrations for $SiO_2$ nanospheres with different diameters. (c-f) Binary mixture of 87 nm and 112 nm $SiO_2$ nanospheres with different mixing ratios: (c) fitted probability density function, (d) digital photos, (e) reflection spectra, and (f) the assembly times and calculated variances.

Thick EDL offers an additional advantage of lower uniformity requirements for $SiO_2$ nanospheres, which is typically necessary to fabricate high-quality colloidal photonic crystals using nanospheres with thin EDL. In our case, where the particle separation is much greater than the diameter of the nanospheres, non-uniform sizes have a negligible impact on the order of assembled crystals. Taking advantage of this benefit, we mixed $SiO_2$ nanospheres with two different diameters in different ratios. The number ratio of the binary mixtures can be estimated based on the diameters, concentrations, and volumes (see Methods section), and Figure 9c displays the fitted distribution of nanospheres in the mixture of 87 nm (6.03 wt.%) and 112 nm $SiO_2$ (5.29 wt.%) (see Figure S17 for TEM). All mixtures had the appearance of assembled photonic crystals in the dispersion (Figure 9d), and the primary diffraction wavelength had a continuous red shift with the addition of more 112 nm $SiO_2$ with 87 nm $SiO_2$ (Figure 9e). A noteworthy observation is that the mixed samples had a narrower diffraction peak than the unmixed ones. This phenomenon can likely be attributed to the formation of crystal structures beyond the BCC lattice within binary mixtures. As demonstrated in previous studies using dynamical diffraction theory, the half-width of the diffraction peak is indeed related to the crystal structure.[21, 36] Experimental efforts are underway to validate and unveil the intricate assembly of structures within these complex conditions.

Regarding the assembly dynamics, samples with higher variances typically require more time to complete the assembly process. This phenomenon in Figure 9f is consistently observed in the other two sets of mixtures (Figure S18: 87 nm & 102 nm, and Figure S19: 87 nm & 120 nm). The positive relation between assembly time and size difference may be attributed to the fact that non-uniform nanospheres require more time to find their respective equilibrium positions. For example, it takes approximately two days for the 87 nm and 120 nm particle mixture to assemble. Despite the slower assembly rate, the formation of colloidal photonic crystals is still observed, indicating the high tolerance of building blocks with thick EDL to size nonuniformity during self-assembly.

## Conclusion

We demonstrate that long-range electrostatic interactions of colloidal silica nanospheres could be effectively established by acid treatment to enable their assembly into colloidal crystals at very low concentrations. Conventionally, the assembly of colloidal $SiO_2$ nanospheres is limited to high particle concentrations due to the thin EDL resulting from the slow release of $NH_4^+$ entrapped during their original synthesis. This acid-treatment method removes the entrapped $NH_4^+$, providing a unique and effective solution for assembling sol-gel-derived $SiO_2$ nanostructures by reducing the electric shielding and enhancing the EDL thickness. It makes silica nanospheres a viable alternative to more popular PS nanospheres as the building blocks for creating colloidal photonic crystals. Compared with other methods employed to increase the EDL thickness for PS nanospheres, such as dialysis,[25] the acid-treatment method is time-efficient and does not require special instruments (i.e., ion-exchange column or resin bed).

In contrast to cases where high particle concentrations typically lead to the formation of FCC colloidal crystals, the increased EDL thickness allows the assembly of $SiO_2$ nanospheres into a BCC lattice at a considerably low particle concentration. This long-range electrostatic repulsion also enables a wide wavelength tunability from visible to near-infrared and high tolerance in size polydispersity of the building blocks for ordering. Further, we reveal that colloidal crystallization at low concentrations involves a disorder-order transition without any significant change in density, and the optimal concentration for crystal formation is governed by both thermodynamic and kinetic factors. Excessively low concentrations result in a heightened interparticle separation, impeding the effective maintenance of the crystal lattice, while excessively high concentrations elevate the kinetic energy barrier required for defect correction. The successful establishment of effective long-range interactions among colloidal silica nanospheres, coupled with the newfound insights into their assembly mechanisms, ushers in a realm of exciting prospects. These advances can effectively facilitate the design and functionalization of silicon-based photonic crystals, thereby extending their applications into uncharted territories.

## Methods

Materials:

The materials and reagents were purchased and used without further purification: Tetraethyl orthosilicate (TEOS, Aldrich, >99%), Ethanol (Koptec, 200 Proof, anhydrous), Ammonium hydroxide ($NH_4OH$, Fisher Chemical, 28 wt.%), HCl (Fisher Chemical, 36.5~38 wt.%). Water was purified through a purification cartridge to reach a resistivity of 18.2 MΩ•cm (25 °C).

Instruments:

UV-VIS spectroscopy: Back reflection spectra were measured by the spectrometer FLAME-S-XR1-ES made by Ocean Optics. The spectra were measured from 365 to 1030 nm with a resolution of 0.5 nm.

Transmission Electron Microscope (TEM): TEM images of nanoparticles were taken on a Thermo Scientific Talos L120C TEM equipped with a Thermo Scientific CETA 16 4Kx4K CMOS camera.

pH meter: The pH of the solutions was measured using a Fisherbrand accumet AB15 Basic benchtop pH meter.

Conductivity meter: The conductivities of the solutions were measured using the OHAUS Bench conductivity meter a-AB23EC.

Zeta potential: Zeta potential of $SiO_2$ nanospheres was measured using Malvern Nano-ZS90.

Small-angle X-ray scattering (SAXS): SAXS data were collected at beamline 7.3.3 of the Advanced Light Source at Lawrence Berkeley National Laboratory. X-rays of wavelength 1.24 Å (10 keV) were used. The sample angle was calibrated with a silver behenate standard. The X-ray beam passed through the sample filled in a flat glass tube, and the scattered radiation was detected with a CCD area detector 3.5 m away from the sample. 1D SAXS data was obtained via an azimuthal average of the 2D scattering patterns. The simulated scattering intensity and structural factor were calculated using the algorithm developed by Lee et al., and the detail of the algorithm was described in the reference.[37] In the calculation, the radius of the nanospheres was set to 42 nm with a polydispersity of 10%. A special note about the photonic crystals can be observed in the sample with a concentration higher than 10 wt.% in the SAXS test (i.e., 13.83 wt.%) is that the SAXS test was carried out over 6 months after the sample was prepared. The increase of ionic strength due to the release of residual $NH_4^+$ ions is anticipated during this long period of storage time. The suitable concentration of ~3-10 wt.% for fast assembly is valid for fresh samples.

Synthesis of $SiO_2$ nanospheres: To synthesize $SiO_2$ nanospheres with an average diameter of 84 nm, 196 mL ethanol, 20 mL Millipore water, and 2.2 mL$NH_4OH$ (28 wt.%) were mixed in a 250 mL flask. After magnetic stirring for 5 min, 10 mL of TEOS was injected. The mixture was maintained at room temperature for 15 h with stirring (300 rpm). The nanospheres were separated from the reaction mixture by centrifuging at 11000 rpm for 15 min. The product was further purified with ethanol twice and water twice to remove any reaction residues. The amount of $NH_4OH$ added was adjusted to control the size of the obtained nanospheres: ~100 nm, ~110 nm, ~120 nm, and ~140 nm nanospheres were obtained using 2.4 mL, 2.5 mL, 2.6 mL, and 2.8 mL of $NH_4OH$. For 350 nm $SiO_2$ nanospheres, 28 mL EtOH, 15 mL $H_2O$, and 7 mL $NH_4OH$ were mixed.

After stirring for 5 min, the mixture of 4.5 mL TEOS and 45 mL EtOH was added. The reaction was stirred at RT for 15 h (300 rpm). The purification procedures were the same as above except for the lower centrifugation speed (7000 rpm for 5 min).

Fabrication of liquid photonic crystals by acid treatment: $SiO_2$ nanospheres were dispersed in 50 mL of water, followed by the addition of HCl solution (1 M) to adjust the pH of the dispersion to ~2.5. The above dispersion was kept under stirring at room temperature for 15 h. Then, the nanospheres were separated from the original acid treatment solution by centrifugation and redispersed in 60 mL of fresh $H_2O$ with the aid of sonication. The dispersion obtained at this stage was named the dispersion with a washing cycle 0. The same centrifugation and redispersion using $H_2O$ was repeated three times. The pH and conductivity were measured when the $SiO_2$ nanoparticles were fully dispersed in the $H_2O$ in each washing cycle. The waiting time for the pH and conductivity measurement was ~15 min (10 min of sonication included), and the concentration of the samples was ~3 wt.%. More detailed information on the treatment duration and time-dependent ion release can be found in the SI. Photonic crystals will form in the solution when the nanospheres are fully dispersed in 35~40 mL of water.

Computational model and analysis:

Interparticle separation: The average interparticle separation (center-to-center) of the whole solution based on volume fraction is calculated based on the equation reported in the literature:[38]

$$CCD = 2r\left[\left(\frac{\phi_m}{\phi}\right)^{\frac{1}{3}} - 1\right]$$

Where $r$ is the radius of the nanosphere, $\phi_m$ is the maximum packing fraction, and $\phi$ is the volume fraction of the colloidal suspension. The maximum packing fraction for crystalline packing (BCC) and random dense packing are 0.68 and 0.63.

The diffraction wavelength due to a specific crystal facet in a crystalline domain is calculated using Bragg's law:

$$\lambda = 2n_{eff} * d_{hkl} * sin\,\theta_{hkl}$$

Where $n_{eff}$ is the effective refractive index of the solution, $d_{hkl}$ is the interplanar distance, and $sin\,\theta_{hkl}$ is the incident angle. Since spectra measured the back reflection, $sin\,\theta_{hkl} = 1$.

For cubic lattices,

$$d_{hkl} = \frac{a}{\sqrt{h^2 + k^2 + l^2}}$$

Therefore,

$$\frac{1/\lambda_1}{1/\lambda_2} = \frac{\sqrt{h_1^2 + k_1^2 + l_1^2}}{\sqrt{h_2^2 + k_2^2 + l_2^2}}$$

The interparticle separation among nanospheres in the crystalline domain can be calculated based on the simple geometry from the calculated interplanar distance.

Electrostatic interaction: The electrostatic interaction between two charged spherical particles was given by the electrical double layer (EDL) potential based on DLVO (DerjaguinLandau-Verwey-Overbeek) theory. The EDL potential between two identical spheres is calculated using the linear superposition approximation (LSA) method:[39, 40]

$$U_{EDL,\,LSA} = \frac{64\pi\varepsilon_0\varepsilon_r r^2\gamma^2}{H}\left(\frac{k_B T}{e}\right)^2 exp\,(-\kappa(H - 2r))$$

In which

$$\gamma = tanh\left(\frac{e\psi}{4k_B T}\right)$$

And for a symmetric monovalent electrolyte:[41]

$$\kappa^{-1} = \sqrt{\frac{\varepsilon_0\varepsilon_r RT}{2000e^2N_A^2 c}}$$

Where $\varepsilon_0$ is the vacuum permittivity, $\varepsilon_r$ is the relative dielectric permittivity of the solvent, $r$ is the radius of the sphere, $H$ is the center-to-center distance between two spheres, $k_B$ is Boltzmann constant, T is absolute temperature, e is the electronic charge, $\kappa$ is the inverse Debye screening length, $\psi$ is the surface potential of the spheres (which has a higher value than zeta potential), $R$ is the gas constant, $N_A$ is the Avogadro constant and $c$ is the electrolyte concentration.

Van Der Waals interaction: The attractive van der Waals interaction between two identical spheres was calculated using:[40, 42]

$$U_{VDW}^{Hamaker} = -\frac{A_H}{6}\left(\frac{2r^2}{H^2 - 4r^2} + \frac{2r^2}{H^2} + ln\left(\frac{H^2 - 4r^2}{H^2}\right)\right)$$

where $A_H$ is the Hamaker constant. For $SiO_2$ in water, it has the value of $8.49*10^{19}$ J.[43]

Steric interaction: A short-range repulsive interaction is considered to resist the attractive van der Waals force when two spheres are very close to each other. Here we use the potential due to the contact of surface ligands to represent the steric repulsion:[44]

$$U_s = 2\pi r^2 N_s k_B T\left[2 - \frac{H - 2r}{\delta} - \frac{H}{\delta} ln\left(\frac{2r + 2\delta}{H}\right)\right] \quad H \leq 2\delta$$

Where $N_s$ is the surface density of surfactant molecules and $\delta$ is the thickness of the surfactant layer.

Static simulation:

Unit cell: the lattice constant of BCC unit cell (a) is calculated by:

$$a = \sqrt[3]{\frac{8\pi}{3\phi}} * r$$

Distorted BCC lattice: the distorted structure is obtained by adding a displacement to each nanosphere in the original BCC lattice. For ith nanosphere:

$$x_{i,\,distorted} = x_{i,origional} + \Delta x_i$$

The displacements ($\Delta x$) are generated following the normal distribution with mean of 0 and sigma of rdm*a. Rdm (0~1) is the parameter that determines the randomness of the distorted lattice.

Unless specified explicitly, the word "potential" in this article refers to the total potential of the system, namely, the sum of the electrostatic, VDW, and steric potentials of all spheres.

Dynamic simulation:

A coarse-grained dynamic simulation model was adopted here to simulate the assembly behavior of $SiO_2$ nanospheres.[44] The model is based on Langevin dynamics and takes into account the electrostatic interaction, van der Waals interaction, steric effect, Brownian diffusion, and hydrodynamic force. In this model, the motion of each particle is governed by a stochastic ODE of the form:

$$m_i \frac{d^2 x_i}{dt^2} + D \frac{dx_i}{dt} = F_{B,\,i} + \sum_{j=1\; j\neq i}^{N} \left(F_{EDL,ij} + F_{VDW,\,ij} + F_{S,\,ij}\right)$$

Where $m_i$ and $x_i$ are the mass and position of the $i$th particle. The second term in the left-hand side of eq 1 represents the viscous (Stokes) drag force, with $D = 6\pi\eta R_{hyd}$ as the drag coefficient ($\eta$ is the fluid viscosity and $R_{hyd}$ is the hydrodynamic radius of the particle). $F_{B,\,i}$ is the stochastic force to account for Brownian motion, and the summation term accounts for interparticle interactions: $F_{EDL,ij}$ the electrostatic force due to electric double layers, $F_{VDW,\,ij}$ the van der Waals force, and $F_{S,\,ij}$ a repulsive force accounting for the steric interaction. These interparticle forces give rise to a coupled system of ODEs, one equation for each colloidal particle. The system of second-order equations was reduced to a system of two coupled first-order equations for the velocity and displacement of the particles. We solve these using a dynamic time-stepping approach that greatly accelerates and stabilizes the solution. The discretized coupled equations are as follows:

$$v_{i,f} = \frac{F_{sum,i}}{D} + \left(v_{i,0} - \frac{F_{sum,i}}{D}\right) e^{-\frac{D}{m_i}\Delta t}$$

$$\Delta x_i = \frac{F_{sum,i}}{D}\Delta t + \frac{m_i}{D}\left(v_{i,0} - \frac{F_{sum,i}}{D}\right)\left(1 - e^{-\frac{D}{m_i}\Delta t}\right)$$

$\Delta t$ is the integration time step, $v_{i,0}$ and $v_{i,f}$ are the velocity of the ith particle at the beginning and end of the time step, and

$$F_{sum,i} = F_{B,\,i} + \sum_{j=1\; j\neq i}^{N} \left(F_{EDL,ij} + F_{VDW,\,ij} + F_{S,\,ij}\right)$$

In our analysis $\Delta t$ was dynamically adjusted based on the displacement to ensure $\Delta x_i < 5$ nm. Except for the Brownian force, all other forces are obtained by taking the gradient of the corresponding potentials. The analytical forms of those forces are given in the supporting information.

Brownian motion: The Brownian force in one dimension was modeled as:

$$F_{B,i} = \sqrt{\frac{2Dk_BT}{\Delta t}}$$

Except for the closed boundary condition, there are two additional layers of BCC lattices outside the simulation box to induce the formation of BCC (Figure S20). The code of potential calculation and dynamic simulation can be found in Zenodo.[45]

Variance of two mixtures: For a colloidal dispersion with a given concentration, the number of nanospheres can be calculated as:

$$N = \frac{wt\,\% * V_{sol} * \rho_{sol}}{\rho_{NS} * \frac{4}{3}\pi * {r_{avg}}^3}$$

where $wt\,\%$, $V_{sol}$, and $\rho_{sol}$ are the weight percent, the volume and the density of the colloidal dispersion, respectively. $\rho_{NS}$ and $r_{avg}$ are the density and average radius of the nanospheres, respectively.

When two dispersions containing nanospheres of different sizes were mixed, if they have similar concentrations, the resulting assumptions are: $\rho_{sol,1} \approx \rho_{sol,2}$, $\rho_{NS,1} \approx \rho_{NS,2}$, then $N \propto \frac{wt\,\% * V_{sol}}{r_{avg}^3}$.

The variance of a mixture of two normal distributions is:

$$\sigma_{1+2} = n_1\sigma_1^2 + n_2\sigma_2^2 + [n_1\mu_1^2 + n_2\mu_2^2 - (n_1\mu_1 + n_2\mu_2)^2]$$

Where $n$, $\mu$, and $\sigma$ are the weights, mean, and sigma of the two normal distributions.

## Supporting Information

Zeta potentials, additional optical images, TEM images, UV-vis spectra, SAXS patterns, parameters in the dynamic simulation, and structural analysis.

Video S1: Dynamic assembly of colloidal photonic crystals in dispersion of different concentrations.

Video S2: Simulated disorder-order transition of nanospheres.

## Acknowledgements

The authors are grateful for the financial support from the U.S. National Science Foundation (CHE-2203972). Q.F. thanks Xiaojing Weng, Zhongxiang Wang, Dr. Ji Feng, Dr. Shiyou Xu, Dr. Bryant Doss, and Dr. Jianzhong Wu for the helpful discussion.

**References:**

1. Krieger, I. M.; O'Neill, F. M., Diffraction of light by arrays of colloidal spheres. *J. Am. Chem. Soc.* **1968,** *90* (12), 3114-3120.
2. Hiltner, P. A.; Krieger, I. M., Diffraction of light by ordered suspensions. *J. Phys. Chem.* **1969,** *73* (7), 2386-2389.
3. Hiltner, P.; Papir, Y.; Krieger, I., Diffraction of light by nonaqueous ordered suspensions. *J. Phys. Chem.* **1971,** *75* (12), 1881-1886.
4. Monovoukas, Y.; Gast, A. P., The experimental phase diagram of charged colloidal suspensions. *J. Colloid Interface Sci.* **1989,** *128* (2), 533-548.
5. Gast, A. P.; Monovoukas, Y., A new growth instability in colloidal crystallization. *Nature* **1991,** *351* (6327), 553-555.
6. Monovoukas, Y.; Gast, A. P., A study of colloidal crystal morphology and orientation via polarizing microscopy. *Langmuir* **1991,** *7* (3), 460-468.
7. Liu, L.; Li, P.; Asher, S. A., Fortuitously superimposed lattice plane secondary diffraction from crystalline colloidal arrays. *J. Am. Chem. Soc.* **1997,** *119* (11), 2729-2732.
8. Holtz, J. H.; Asher, S. A., Polymerized colloidal crystal hydrogel films as intelligent chemical sensing materials. *Nature* **1997,** *389* (6653), 829-832.
9. Lee, K.; Asher, S. A., Photonic crystal chemical sensors: pH and ionic strength. *J. Am. Chem. Soc.* **2000,** *122* (39), 9534-9537.
10. Asher, S. A.; Sharma, A. C.; Goponenko, A. V.; Ward, M. M., Photonic crystal aqueous metal cation sensing materials. *Anal. Chem.* **2003,** *75* (7), 1676-1683.
11. Reese, C. E.; Asher, S. A., Photonic crystal optrode sensor for detection of Pb2+ in high ionic strength environments. *Anal. Chem.* **2003,** *75* (15), 3915-3918.
12. Zhang, Y.; Ge, J., Liquid photonic crystal detection reagent for reliable sensing of Cu(2+) in water. *RSC Adv.* **2020,** *10* (18), 10972-10979.
13. Asher, S. A.; Alexeev, V. L.; Goponenko, A. V.; Sharma, A. C.; Lednev, I. K.; Wilcox, C. S.; Finegold, D. N., Photonic crystal carbohydrate sensors: low ionic strength sugar sensing. *J. Am. Chem. Soc.* **2003,** *125* (11), 3322-3329.
14. Ben-Moshe, M.; Alexeev, V. L.; Asher, S. A. J. A. c., Fast responsive crystalline colloidal array photonic crystal glucose sensors. *Anal. Chem.* **2006,** *78* (14), 5149-5157.
15. Yang, D.; Ye, S.; Ge, J., Solvent wrapped metastable colloidal crystals: highly mutable colloidal assemblies sensitive to weak external disturbance. *J. Am. Chem. Soc.* **2013,** *135* (49), 18370-6.
16. Zhu, B.; Fu, Q.; Chen, K.; Ge, J., Liquid Photonic Crystals for Mesopore Detection. *Angew. Chem. Int. Ed.* **2018,** *57* (1), 252-256.
17. Juang, M. S. D.; Krieger, I. M., Emulsifier‐free emulsion polymerization with ionic comonomer. *J. Polym. Sci., Part A: Polym. Chem.* **1976,** *14* (9), 2089-2107.
18. Reese, C. E.; Guerrero, C. D.; Weissman, J. M.; Lee, K.; Asher, S. A., Synthesis of Highly Charged, Monodisperse Polystyrene Colloidal Particles for the Fabrication of Photonic Crystals. *J. Colloid Interface Sci.* **2000,** *232* (1), 76-80.
19. Stöber, W.; Fink, A.; Bohn, E., Controlled growth of monodisperse silica spheres in the micron size range. *J. Colloid Interface Sci.* **1968,** *26* (1), 62-69.
20. Han, Y.; Lu, Z.; Teng, Z.; Liang, J.; Guo, Z.; Wang, D.; Han, M. Y.; Yang, W., Unraveling the Growth Mechanism of Silica Particles in the Stober Method: In Situ Seeded Growth Model. *Langmuir* **2017,** *33* (23), 5879-5890.

21. Rundquist, P. A.; Photinos, P.; Jagannathan, S.; Asher, S. A., Dynamical Bragg diffraction from crystalline colloidal arrays. *J. Chem. Phys.* **1989,** *91* (8), 4932-4941.

22. Li, Y.; Fan, Q.; Wang, X.; Liu, G.; Chai, L.; Zhou, L.; Shao, J.; Yin, Y., Shear‐Induced Assembly of Liquid Colloidal Crystals for Large‐Scale Structural Coloration of Textiles. *Adv. Funct. Mater.* **2021,** *31* (19), 2010746.

23. Huang, C.; Shang, Y.; Hua, J.; Yin, Y.; Du, X., Self-Destructive Structural Color Liquids for Time-Temperature Indicating. *ACS Nano* **2023,** *17* (11), 10269-10279.

24. Asher, S. A.; Weissman, J. M.; Tikhonov, A.; Coalson, R. D.; Kesavamoorthy, R., Diffraction in crystalline colloidal-array photonic crystals. *Phys. Rev. E* **2004,** *69* (6), 066619.

25. Carlson, R. J.; Asher, S. A., Characterization of optical diffraction and crystal structure in monodisperse polystyrene colloids. *Appl. Spectrosc.* **1984,** *38* (3), 297-304.

26. Wong, Y. J.; Zhu, L.; Teo, W. S.; Tan, Y. W.; Yang, Y.; Wang, C.; Chen, H., Revisiting the Stober method: inhomogeneity in silica shells. *J. Am. Chem. Soc.* **2011,** *133* (30), 11422-5.

27. Song, X.; Ding, T.; Yao, L.; Lin, M.; Siew Tan, R. L.; Liu, C.; Sokol, K.; Yu, L.; Lou, X. W.; Chen, H., On the Origin and Underappreciated Effects of Ion Doping in Silica. *Small* **2015,** *11* (34), 4351-65.

28. García, P. D.; Sapienza, R.; Blanco, Á.; López, C., Photonic Glass: A Novel Random Material for Light. *Adv. Mater.* **2007,** *19* (18), 2597-2602.

29. Shang, G.; Maiwald, L.; Renner, H.; Jalas, D.; Dosta, M.; Heinrich, S.; Petrov, A.; Eich, M., Photonic glass for high contrast structural color. *Sci. Rep.* **2018,** *8* (1), 7804.

30. Ma, H.; Liu, Y., Photonic glass based structural color. *APL Photonics* **2020,** *5* (6), 060901.

31. Ehrlich, G.; Hudda, F. G., Atomic view of surface self‐diffusion: tungsten on tungsten. *J. Chem. Phys.* **1966,** *44* (3), 1039-1049.

32. Schwoebel, R. L.; Shipsey, E., Step motion on crystal surfaces. *J. Appl. Phys.* **1966,** *37* (10), 3682-3686.

33. e Silva, J. M.; Mokross, B., Solidlike phase transitions in a screened Wigner lattice. Statics. *Phys. Rev. B* **1980,** *21* (7), 2972.

34. Beunen, J. A.; White, L. R., The order-disorder transition in latex dispersions. *Colloids Surfaces* **1981,** *3* (4), 371-390.

35. Chaikin, P.; Pincus, P.; Alexander, S.; Hone, D., BCC-FCC, melting and reentrant transitions in colloidal crystals. *J. Colloid Interface Sci.* **1982,** *89* (2), 555-562.

36. Spry, R. J.; Kosan, D., Theoretical analysis of the crystalline colloidal array filter. *Appl. Spectrosc.* **1986,** *40* (6), 782-784.

37. O'Brien, M. N.; Jones, M. R.; Lee, B.; Mirkin, C. A., Anisotropic nanoparticle complementarity in DNA-mediated co-crystallization. *Nat. Mater.* **2015,** *14* (8), 833-839.

38. Hao, T.; Riman, R. E., Calculation of interparticle spacing in colloidal systems. *J. Colloid Interface Sci.* **2006,** *297* (1), 374-7.

39. Bell, G.; Levine, S.; McCartney, L., Approximate methods of determining the double-layer free energy of interaction between two charged colloidal spheres. *J. Colloid Interface Sci.* **1970,** *33* (3), 335-359.

40. Bhattacharjee, S.; Elimelech, M.; Borkovec, M., DLVO interaction between colloidal particles: Beyond Derjaguin’s approximation. *Croat. Chem. Acta* **1998,** *71* (4), 883-903.

41. Berg, J. C., *An introduction to interfaces & colloids: the bridge to nanoscience*. World Scientific: 2010.

42. Hamaker, H. C., The London—van der Waals attraction between spherical particles. *physica* **1937,** *4* (10), 1058-1072.

43. Hough, D. B.; White, L. R., The calculation of Hamaker constants from Liftshitz theory with applications to wetting phenomena. *Adv. Colloid Interface Sci.* **1980,** *14* (1), 3-41.

44. Xue, X.; Furlani, E. P., Analysis of the Dynamics of Magnetic Core–Shell Nanoparticles and Self-Assembly of Crystalline Superstructures in Gradient Fields. *J. Phys. Chem. C* **2015,** *119* (10), 5714-5726.

45. Fan, Q. Potential Calculation and Dynamic Simulation of BCC Photonic Crystals Assembled from SiO2 Nanospheres. In Unveiling Enhanced Electrostatic Repulsion in Silica Nanosphere Assembly: Formation Dynamics of Body-Centered-Cubic Colloidal Crystals. Zenodo. 2023, https://doi.org/10.5281/zenodo.10055437 (accessed 2023-11-01).

TOC Graphic: